Designed 3D Dumpling-Shaped Femtosecond Laser Structured Light Field for Nanoscale Sensing

Deng Pan, Zhijuan Fuyang, Hui Wang, Zhiqiang Wang,* Yan Kuai, Chenchu Zhang, Zhaoxin Lao, Jingjing Zhang,* Jincheng Ni, Bing Xu, Shenglai Zhen, Benli Yu, and Dong Wu*

Nanoscale optical sensing plays a crucial role in achieving high-precision non-contact distance and displacement measurements. As one of the promising alternatives, structured light can greatly simplify optical sensing systems. In this study, a novel optical phenomenon of a structured beam called the "Dumpling-shaped Structured Light Field" (DSLF) is revealed, which forms during the focusing of cylindrical lens beams. The 3D DSLF comprises two mutually perpendicular primary and secondary foci, offering unique possibilities in micro/nano processing and sensing applications. A thorough investigation of the DSLF is conducted, revealing a correlation between the secondary foci and the phase status at the objective lens's entrance pupil. The propagation of DSLF under tight focus conditions has been verified and discussed through methods of femtosecond laser two-photon polymerization and light field analysis. Finally, thanks to the unique 3D intensity distribution of 3D DSLF, the applicability of DSLF in high-precision position and vibration sensing has been demonstrated. By detecting the horizontal and vertical dimensions of the reflected DSLF, position and vibration sensing is achieved with a Z-direction accuracy of 10 nm (λ/80). This research contributes to understanding structured light, and offers practical applications in various fields, including micro/nano laser processing, optical imaging, sensing, etc.

1. Introduction

Benefiting from the abundant measurable parameters and the flexible control characteristics of light, nanoscale optical sensing is of particular significance for it achieves high-precision non-contact distance and displacement measurements, and are widely used in fields such as microscopy, mechanical engineering, quantum physics, and semiconductor manufacturing.[1–4] The interferometric technique, a key player in achieving minute displacement detection by capturing relative phase differences, has witnessed considerable progress.[5] However, its efficacy comes at the cost of intricate interference systems, imposing stringent demands on measurement setups. Recognizing this, tremendous efforts have been dedicated to continuously advancing the novel nanoscale optical sensing technologies. For instance, a novel approach involves leveraging the response of nano dielectric particles to the local polarized light of a structured optical field,

D. Pan, Z. Fuyang, H. Wang, Z. Wang, Y. Kuai, S. Zhen, B. Yu
Information Materials and Intelligent Sensing Laboratory of Anhui Province
Anhui University
111 Jiu Long Road, Hefei 230601, China
E-mail: zhiqiangwang@ahu.edu.cn
C. Zhang, Z. Lao
Hefei University of Technology
Hefei 230009, China
J. Zhang
School of Mathematical Sciences
Anhui University
111 Jiu Long Road, Hefei 230601, China
E-mail: jjmath@ahu.edu.cn

J. Ni, D. Wu
Hefei National Laboratory for Physical Sciences at the Microscale
CAS Key Laboratory of Mechanical Behavior and Design of Materials
Department of Precision Machinery and Precision Instrumentation
University of Science and Technology of China
Hefei, Anhui 230027, China
E-mail: dongwu@ustc.edu.cn
B. Xu
School of Mechanical Engineering
Suzhou University of Science and Technology
Suzhou 215009, China

**ADVANCED
SCIENCE NEWS**

www.advancedsciencenews.com

**ADVANCED
FUNCTIONAL
MATERIALS**

www.afm-journal.de

paving the way for innovative displacement sensors.[6–8] Yet, precision in displacement measurement is contingent upon the choice of nanostructures, such as silicon particles, limiting its broad applicability. Another noteworthy alternative involves the use of optical metasurfaces. Yuan and Zheludev's optical ruler, for instance, offers a promising avenue for lateral nanoscale displacement measurements.[9] While this method necessitates an ultrastable laser.[10] Wang et al. recently used the optical metasurfaces to achieve the large-scale and high-sensitivity displacement sensing, which proved a long-range, high-precision, and compact transverse displacement metrology method.[11] Nevertheless, its reliance on optical metasurface components entails the use of relatively costly equipment and intricate manufacturing processes, posing certain constraints on its broader applicability to some extent.

Structured light, including vortex beams, Bessel beams, Airy beams, and others, represents a category of customized optical fields with distinctive spatiotemporal evolution properties, featuring a spatially-varying distribution of amplitude, phase, and/or polarization.[12–18] These structured lights exhibit novel features during interactions with matter and have found wide-ranging applications in areas such as optical manipulation, biomedical imaging, optical sensing, and optical communication.[19–22] In the field of optical sensing, the use of 2D structured light for sensing has found extensive applications with the advantages of simplicity, fast measurement, and high accuracy.[23,24] For example, grid or line-based 2D structured light is projected onto an object, and by employing specific algorithms, the distortions in the returned encoded patterns are computed to derive information.[25] However, the inherent limitation of lacking depth information poses a challenge in achieving nanoscale depth position sensing and measurement.

In this study, we introduce a simple, flexible, and designable 3D structured light for micro/nanoscale fabrication and optical sensing. By employing cylindrical lens phase modulation, we can generate a 3D dumpling-shaped structured light field (DSLF) within a tightly focused environment. The DSLF consists of two mutually perpendicular line-shaped focal points in space, of which the 3D morphology of which can be flexibly controlled. Additionally, we conducted a detailed investigation of the propagation and focusing characteristics of the generated 3D DSLD through a comprehensive optical computation involving scalar and vector fields. Based on theoretical analysis and experimental measurements, our 3D light field exhibits varying intensity profiles at different focusing depths. Furthermore, it has been proven that DSLF is highly applicable in high-precision position and vibration sensing, enabling the detection of 10 nm (λ/80) position changes and vibrations, showing the promising prospect in the field of optical imaging, and nanoscale sensing.

2. Results and Discussion

2.1. The Generation of Dumpling-Shaped Structured Light Field

The generation of DSLF is based on the modulation of cylindrical lens beams. As a kind of structured light,[26] cylindrical lens beams with line-shaped focus have been widely used in many fields such as optical measurement, microscopy, microfabrica-

tion, etc.[27–30] Here, our objective is to construct a 3D structured light field by introducing an additional line-shaped beam beyond the initial line-shaped focal points. We eschew the traditional use of a 4F system as an intermediary between the modulation plane and the entrance pupil of the objective. Instead, we directly employ the objective to focus the light beam. This approach enables us to fully exploit the focusing properties of the cylindrical lens, leading to the generation of a secondary line-shaped focal point.

The generation of the DSLF is achieved through a simple optical setup, as depicted in **Figure 1a**. The femtosecond laser beam first passes through a laser power conditioning module composed of a half-wave plate and a polarizing beam splitter. The laser power can be precisely adjusted by varying the rotation angle of the half-wave plate. Subsequently, the diameter of the laser beam is expanded by a beam expander to match the size of the spatial light modulator (SLM). On the SLM panel (Figure 1b), holograms with a cylindrical lens phase are loaded. It is worth noting that the SLM device, with the advantage of flexibility,[31] can be substituted by other optical modulation devices (including cylindrical lenses, diffraction elements, etc.) capable of generating cylindrical phase. As the laser beam is reflected by the SLM, the beam phase is modulated into the cylindrical lens phase, which generates a line-shaped light field in the free space. The phase of a cylindrical lens beam can be written as:

$$\varphi(u, v) = \frac{2\pi}{\lambda} \frac{u^2}{2f} \tag{1}$$

where the λ is the wavelength, and the f is the focusing length of the cylindrical lens beam. u and v are the horizontal and vertical coordinates of the phase plane. Here we use a high NA objective lens (OL) to further focus the line-shaped light field. Due to the tight focusing effect of high numerical aperture (NA) objective lenses, the line-shaped light field in the free space will generate an additional secondary focus perpendicular to the primary focus, either in front of or behind the focus plane of the objective lens. These two linear light fields collectively form the distinctive DSLF. Figure 1c shows the 3D intensity distribution of the DSLF, where the red, green, and blue regions indicate light intensity values at 5%, 30%, and 70% of the maximum intensity, respectively.

Two critical parameters dictate the ultimate shape of the light field. First, the distance between the SLM and OL (denoted as "d") is calculated by adding the distance from the SLM to the diffraction mirror (DM) (referred to as "d_1") and the distance from the DM to the pupils of the OL (referred to as "d_2"). Second, the focal length of the cylindrical beam (f) determines the focusing position of the cylindrical lens beams in free space. The relationship between d and f is a crucial condition for modulating the beam shape of the DSLF, which will be discussed in detail below.

To collect the generated light field, a reflecting mirror is positioned beneath the OL. The mirror's space position is controlled by a piezoelectric ceramic 3D motion platform with 0.1 nm open-loop control accuracy. Besides, an imaging system consisting of a lens and a charge-coupled device (CCD) is utilized to capture the images.
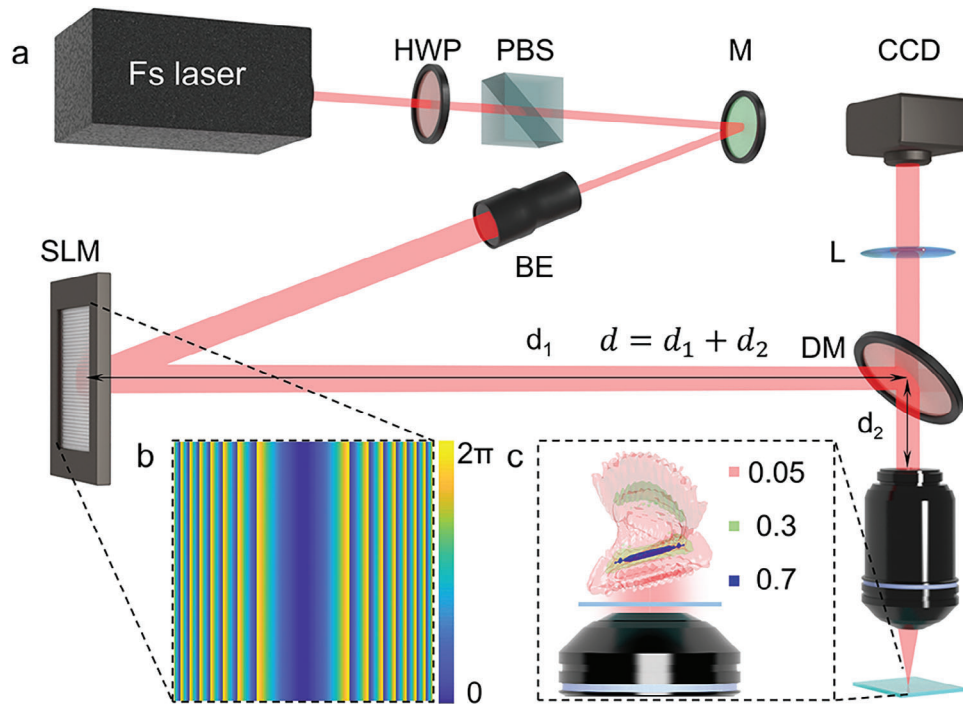
Figure 1. The optical system for generating the 3D dumpling-shaped beam. a) Experiment setup: Fs laser, femtosecond laser; HWP, half-wave plate; PBS, polarizing beam splitter; M, mirror; BE, beam expander; SLM, spatial light modulator; DM, dichroic mirror; OL, objective lens; L, lens; CCD, charge coupled device. b) The only-phase hologram of a cylindrical lens loaded on the SLM. c) The designed DSLF is generated after focusing by an objective lens.

2.2. The Propagation and Focusing Process of DSLF

The generation of the DSLF involves two distinct processes: propagation in free space and tight focusing under a high NA objective lens. In order to facilitate comprehensive light field calculations, we simplify the entire optical path to the model illustrated in **Figure 2a**. The plane denoted as "Q" corresponds to the modulation plane of the SLM. As the incident beam illuminates the rear aperture of the objective lens (denoted as P_i), the wavefront of the incident beam is refracted by the High NA OL, transforming into a converging spherical surface (denoted as Pr). Subsequently, structured beams are generated through the superposition of all the wavelets within the maximum convergence angle, and the origin of the coordinate system XYZ is located at the focal point of the OL.

The propagation process of the DSLF from plane Q to plane P_i can be described by the scalar Rayleigh–Sommerfeld diffraction integral:

$$E\left(u', v', d\right) = -\frac{i}{\lambda} \iint_{\Omega} E_0\left(u, v, 0\right) \times \frac{\exp\left(ikr\right)}{r} \times \cos\theta \, du \, dv \quad (2)$$

where $r = \sqrt{\left(u' - u\right)^2 + \left(v' - v\right)^2 + d^2}$, $k = 2\pi/\lambda$, u' and v' are the horizontal and vertical coordinates of the rear focal plane of objective lens. d is the distance from plane Q to plane P_i. In the actual optical system, the distance from Q to P_i greatly exceeds the size of the diffraction plane. Therefore, Equation 1 can be simpli-

fied with the Fresnel approximation, that is, $r \approx d + \frac{\left(u' - u\right)^2 + \left(v' - v\right)^2}{2d}$. Moreover, in the paraxial approximation condition $\cos\theta = 1$ can be ensured. By this means, the complex electric field (E) in the plane P_i can be written as:

$$E\left(u', v', d\right) = \frac{\exp\left(ikd\right)}{i\lambda d} \iint_{\Omega} E_0\left(u, v, 0\right)$$

$$\times \exp\left\{\frac{ik}{2d}\left[\left(u' - u\right)^2 + \left(v' - v\right)^2\right]\right\} du \, dv \quad (3)$$

Here, the phase of plane Q is a cylindrical lens phase, which will generate a cylindrical beam in free space. The complex electric field of cylindrical beam modulated by plane Q can be described as:

$$E\left(u, v\right) = A_0\left(u, v\right)\exp\left(-ik\frac{u^2}{2f}\right) \quad (4)$$

where A_0 is the amplitude, and f is the focus length of the cylindrical lens phase loaded on the SLM plane. The parameter f determines the line-shaped focus position of laser beam in free space. Different from the common utilization that uses the cylindrical lens for generating a 2D line-shaped focus,[29,32] we find that the system consists of SLM loaded on a cylindrical lens phase and an objective lens can generate 3D spatially structured light fields. The 3D intensity distributions of DSLF are related to the relationships of f and d. In this experimental setup, the distance d is 1600 mm. Therefore, we chose three distinct values for f:
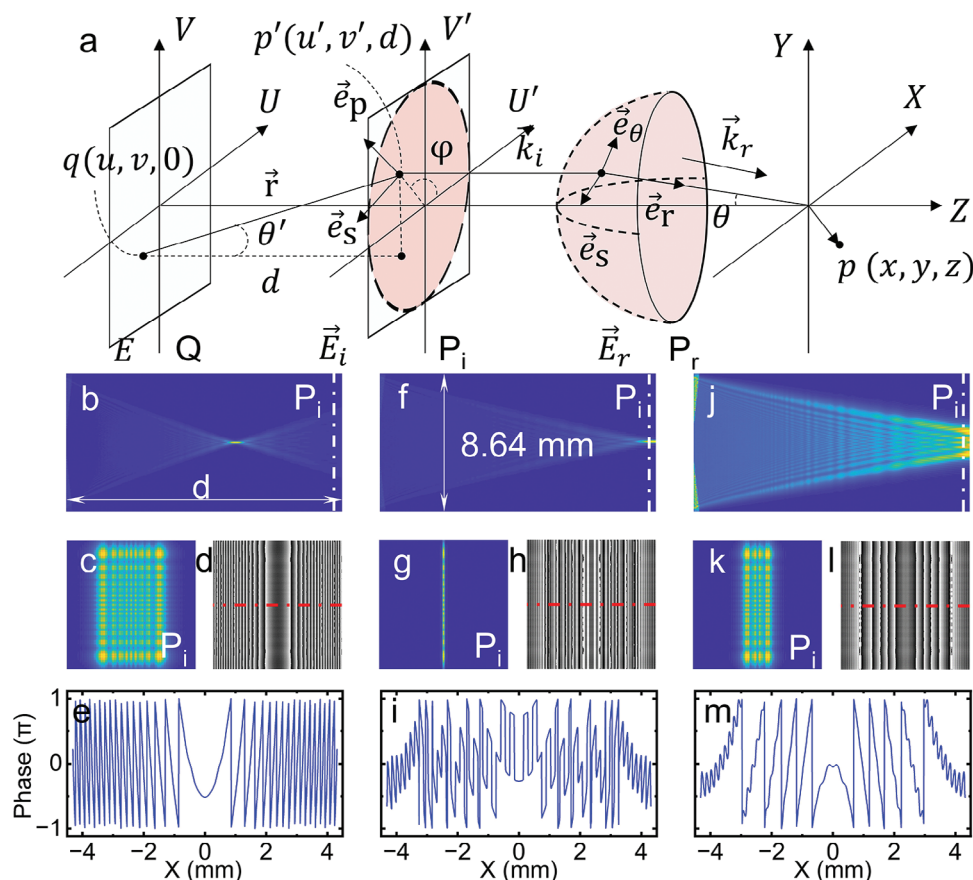
ADVANCED
SCIENCE NEWS
www.advancedsciencenews.com

ADVANCED
FUNCTIONAL
MATERIALS
www.afm-journal.de

Figure 2. The simulated optical propagating properties of the DSLF. a) The optical diffraction model of the designed DLSF. Plane Q, the phase plane; plane P_i, the plane of the objective lens pupil; sphere P_r, the distorting surface of the objective. b,f,j) The intensity distribution of the DLSF focused by f = 1000 mm, f = 1600 mm, and f = 2200 mm in the free space, respectively. c,g,k) The calculated intensity distribution of the DLSF with f = 1000 mm, f = 1600 mm, and f = 2200 mm at plane P_i. d,h,l) the calculated phase distribution of the DLSF with f = 1000 mm, f = 1600 mm, and f = 2200 mm at plane P_i, respectively. e,i,m) the phase curve marked by the red dash line in Figure d, h, and l, respectively.

f = 1000, 1600, and 2200 mm, corresponding to three conditions f<d, f = d, and f>d, respectively.

Specifically, the process of cylindrical beam propagation from Q to P_i can be discussed in three cases: 1) When f is less than d, (f<d), the laser beam will focus in front of plane P_i, and will diverge and propagate forward, resulting in a square beam with a diverging phase illumining on the plane P_i. Here, the light intensity distribution of the cylindrical beam with f = 1000 mm in free space is calculated by Equations 2 and 3, and the results are shown in Figure 2b–e. In the X–Z plane, the calculation results reveal that the cylindrical beam has focused (Figure 2b) before reaching the plane P_i, which is consistent with the theoretical analysis. Figure 2c,d depicts the intensity and phase distribution of the plane P_i, showing a square-shaped beam with a typical cylindrical lens phase. In order to reveal the divergent phases, the phase curve of red dash line in Figure 2d is represented (Figure 2e). It can be clearly seen that the phase curve has an upward opening direction at U = 0, further affirming the divergence of the cylindrical beam. 2) When f equals d (f = d), the cylindrical beam can accurately focus on the plane P_i (Figure 2f). In this situation, a line-shaped focus is generated on plane P_i. The phase shows strong oscillations and can be considered as a

plane wave phase with no divergence or focus at the center of the beam (Figure 2h,i). 3. When f exceeds d (f>d), the cylindrical beam's focal length is larger than d. As the cylindrical beam reaches plane P_i, it is not fully focused yet (Figure 2j), resulting in a square intensity distribution and a convergent phase at the plane P_i (Figure 2k,l). The phase curve of red dash line in Figure 2l shows a downward opening direction at U = 0.

In each case, the behavior of the cylindrical beam is influenced by the relationship between f and d, leading to variations in the DSLF shape and characteristics when focused by the objective lens. When the incident beam is focused by a high NA OL (NA = 0.9, 100×, effective focusing lengths = 1.8 mm), the polarization components are changed under the tight focus condition. Because of the refraction induced by OL, the electric field components (e_p and e_s) at P_i will transform into e_θ, e_s, and e_r, which can be expressed by:

$$\vec{E}_r = A_0 \sqrt{\cos(\theta)} \times M \times \vec{E}_i \tag{5}$$

where $\vec{E}_r = \vec{e}_\theta + \vec{e}_s + \vec{e}_r$, M is the transform matrix, $A_0 \sqrt{\cos(\theta)}$ is the apodization factor, $\vec{E}_i = \vec{e}_p + \vec{e}_s$ is the electric field vector
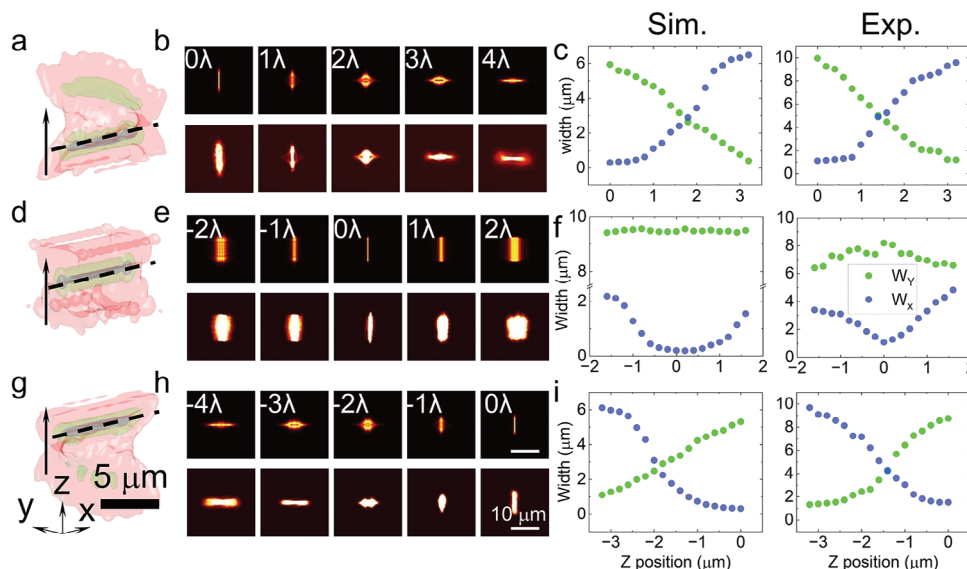
**ADVANCED
SCIENCE NEWS**

www.advancedsciencenews.com

**ADVANCED
FUNCTIONAL
MATERIALS**

www.afm-journal.de

Figure 3. The DLSF generated by a high-NA objective lens. a) The calculated 3D light intensity of DLSF with f = 1000 mm. The black dash line shows the position of objective lens focus. b) The simulated (above) and experimental (below) results of the DLSF with f = 1000 mm, the scale bar is 5 μm. c) The statistics of the DLSF length (f = 1000 mm) in the x (Wx) and y (Wy) directions. d) The calculated 3D light intensity of DLSF with f = 1600 mm. e) the simulated (above) and experimental (below) results of the DLSF with f = 1600 mm. f) The Statistics of the length of the DLSF (f = 1600 mm) in the x (Wx) and y(Wy) directions. g) The calculated 3D light intensity of DLSF with f = 2200 mm. h) the simulated (above) and experimental (below) results of the DLSF with f = 2200 mm. i) the Statistics of the length of the DLSF (f = 2200 mm) in the x (Wx) and y(Wy) directions. The scale bar of (a,d,g) is 5 μm. The scale bar of (b,e,h) is 10 μm.

before transformation. After the transformation, the electric field of imaging point p(x,y,z) can be calculated by the Debye integral formula,

$$\vec{E} = -\frac{iC}{\lambda} \iint_{\Sigma} \vec{E}_r \times \exp\left[i\left(k_z z - k_x x - k_y y\right)\right] d\Sigma \qquad (6)$$

where k_x, k_y, k_z are the wave vector of the electric field in the x, y, z directions. The light intensity distribution of the focused beam can be expressed by $I = E^2$.

Here, we have accurately calculated the 3D spatial light field distribution of the 3D DSLF through full-path optical calculation of scalar and vector diffraction. We calculate the 3D intensity distribution of the structured beam with three typical parameters f = 1000 mm, f = 1600 mm, and f = 2200 mm, where f is the focal length of the cylindrical lens. **Figure 3a** shows the focused beam with a parameter of f = 1000 mm. Interestingly, the 3D shape of the light field bears a resemblance to traditional Chinese food, dumplings. As such, we named this light field the "dumpling-shaped structured light field" (DSLF). DSLF consists of two mutually perpendicular linear beams, one of which is straight and the other is curved. On the one hand, the straight-line beam is located at the position of Z = 0 which is marked by the black dashed line. On the other hand, the curved beam is located at the region of Z<0 (the propagation direction is marked by the black arrow). The phenomenon that a curved beam is formed before straight focus can be attributed to the beam with f = 1000 mm carrying a divergent phase when illuminating in the entrance pupil.

It is worth noting that the length of the DSLF in the horizontal (X) and vertical (Y) directions changes with the propagation distance. We quantitatively analyze the size evolution of the focused beam at high NA, and the results are shown in Figure 3b. When the propagation distance varies from 0 to 4 λ, the spot direction on the X–Y plane changes from vertical to horizontal. The simulation results (above) are consistent with the experimental results (below). Specifically, the length in the X direction (Wx) gradually increases from 300 nm to 6.5 μm as the DSLF propagates, while the length in the Y direction (Wy) gradually decreases from 6 μm to 400 nm (Figure 3c).

As for the DSLF of f = 1600 mm, the incident beam at plane P_i carries a phase similar to the plane wave phase, resulting in the beam precisely focusing at the focal point of the objective lens without generating a second focal point (Figure 3d). The evolution of the generated perfect line-shaped focus is illustrated in Figure 3e. The simulation and experimental results show that during the propagation process from −2 to 2 λ, Wx initially decreases and then increases, reaching a minimum value at the focus (200 nm), while Wy remains unchanged (9.5 μm), showing a typical cylindrical lens focusing process (Figure 3e,f).

The final scenario concerns the DSLF with f = 2200 mm. In this case, the light beam is not fully focused when it illustrates the entrance pupil plane of the objective lens, so it carries a converging phase factor. The shape of the focused beam is similar to dumpling, but the direction is reversed from DSLF with parameters of f = 1000 mm. The converging phase of the DSLF generates a secondary focus behind the focus at Z = 0. Therefore, the focus direction on the X–Y plane changes from horizontal to vertical, causing a decrease in Wx and an increase in Wy (Figure 3h) as the propagation distance increases from −4 to 0 λ. Quantitative data illustrate that the Wx of DSLF with f = 2200 mm decreases

**ADVANCED
SCIENCE NEWS**

www.advancedsciencenews.com

**ADVANCED
FUNCTIONAL
MATERIALS**

www.afm-journal.de

from 6.1 µm to 320 nm, and the Wy increases from 1 to 5.3 µm (Figure 3i).

Overall, the morphology of the DSLF can be precisely tuned by the focusing parameter f (Figure S1 and Videos S1–S3, Supporting Information). According to the theoretical analysis and experimental results of the optical propagation process, the change in the direction of the spherical wave vector is the intrinsic reason for the change in the shape of the DSLF. Additionally, the NA of the objective lens can also regulate the 3D intensity distribution of DSLF. A larger NA of the objective lens leads to shorter lengths of the primary and secondary foci and a smaller z-direction distance between them (Figure S2, Supporting Information). It is worth noting that another alternative DSLF control system is to place a 4f system between the SLM and objective lens, the advantage of this system is that the low-frequency information of the modulation process can be filtered out by the 4f system, but the disadvantage is that it increases the complexity of the system (Figure S3, Supporting Information). We believe that we have introduced a novel method for controlling the secondary focus in DSLF. A combination of theory and experimentation supports our findings, emphasizing the practicality of these methods in various optical applications.

2.3. The Validation of 3D Light Intensity Distribution of DSLD via DSLF Two-Photon Polymerization

To further validate the 3D light intensity distribution and elucidate the light field evolution, a two-photon polymerization experiment was conducted by exposing the photo resist (SZ2080, IESL-FORTH, Greece) with the modulated structured light field.[33] Before the fabrication process, a 170-micron thick glass substrate was coated with photosensitive resist, and organic solvents were removed by heating the substrate on a hot plate at 100 °C for an hour. The side coated with photoresist is faced down, and mineral oil (refractive index 1.518) is dropped on the glass to match the refractive index of objective lens. During the fabrication process, the position is precisely controlled by a 3D ceramic nanopiezoelectric motion platform, the laser intensity is controlled at 50 mW, and the exposure time is set to be 0.5 s per position. After the exposure, the whole photoresist sample is immersed in n-propanol, removing the unexposed area.

As shown in **Figure** 4a–i, three typical DSLF with f = 1000, 1600, and 2200 mm are chosen for fabrication experiments. An oil-immersed objective lens with an NA of 1.35 and effective focusing lengths of 3 mm was utilized for superior processing compared to the 100x objective lens with NA = 0.9. The simulated 3D intensity distribution of DSLF with f = 1000 mm is shown in Figure 4a, showing an upright dumpling shape (Video S4, Supporting Information). Optical images captured at different Z positions during the fabrication process are illustrated in Figure 4b. At the platform position of Z = 0 µm, the vertical microstructure fabricated by the primary focus can be clearly seen. With an increase in exposure depth, the secondary focus exposes horizontal microstructure at Z = 20 µm, which is consistent with the evolution of the DSLF. The SEM image of the exposed microstructure is shown in Figure 4C, confirming the dumpling-like shape of the fabricated microstructure. The micro dumpling size, measuring is 18 µm × 18 µm, is consistent with the calculated results

(Figure 4a), demonstrating the correctness of the theoretical analysis of the DSLF.

When f = 1600 mm, the secondary focus of the DSLF disappears, and only the primary focus remains (Figure 4d). Therefore, as the platform position increases from 0 to 20 µm, only a line-shaped microstructure forms inside the photoresist as shown in Figure 4e. The SEM image of the exposed line-shaped microstructure is shown in Figure 4f. The micro line has a width of 572.2 nm (Figure S4, Supporting Information) and a length of 8.8 µm, showing the typical two-photon polymerization fabrication resolution. In addition, we can reduce the exposure time of each structure to 10 ms by increasing the laser intensity to 500 mW, significantly enhancing the efficiency of processing compared to the conventional point-by-point methods. Besides, the width of the line-shaped microstructures can be further decreased to ≈279 nm by controlling the exposure conditions near the critical threshold of two-photon polymerization. As illustrated in Figure 4l,m, we have successfully fabricated a photoresist periodic structure comprised of 2800 line-shaped microstructures within ≈30 s, thereby underscoring the method's potential for large-scale manufacturing. The periodic structure exhibits vibrant colors when illuminated by a white LED light source, and also demonstrates a typical periodic structure diffraction pattern when illuminated by laser light, as evident in Figure 4n.

As for f = 2200 mm, the simulated result shows that the secondary focus generated behind the primary focus, as per theoretical analysis, generating an upside-down optical dumpling (Figure 4g). Therefore, the horizontal microstructure appears at Z = 0 µm, while the vertical microstructure appears at Z = 20 µm, generating upside-down micro dumpling. Since the micro dumpling structure is inverted (the curved edge is close to the glass substrate), we precisely control the exposure position so that the microstructures do not adhere to the substrate for ensuring the integrity of micro dumplings. The prepared micro dumplings, as shown in Figure 4i, exhibited a structure that inverted onto the substrate due to the lack of adhesion between the structure and the substrate during processing and development.

Furthermore, to provide a clearer depiction of the DSLF's 3D light field profile, we also fabricated a microstructure array with increasing processing heights (Figure 4j). As the processing height gradually increased, the exposure depth of the DSLF also increased, resulting in an increase in the height of the exposed microstructure and a gradual improvement in its completeness (Figure 4k). The height of the final microdumpling structure reached 18 µm, consistent with the results of the light field simulation, further validating the dumpling-shaped profile of the DSLF's 3D light field distribution.

2.4. Microvibration Monitoring with DSLF

To the best of our knowledge, this study presents the first comprehensive investigation of the Dumpling-shaped Structured Light Field. Given that the primary and secondary foci of the DSLF are spatially distributed at a 90° angle and do not coincide in the same plane, the intensity distribution of the light field varies at different spatial positions (as discussed in Figure 3). Therefore, we applied the dumpling beam to the fields of spatial position sensing
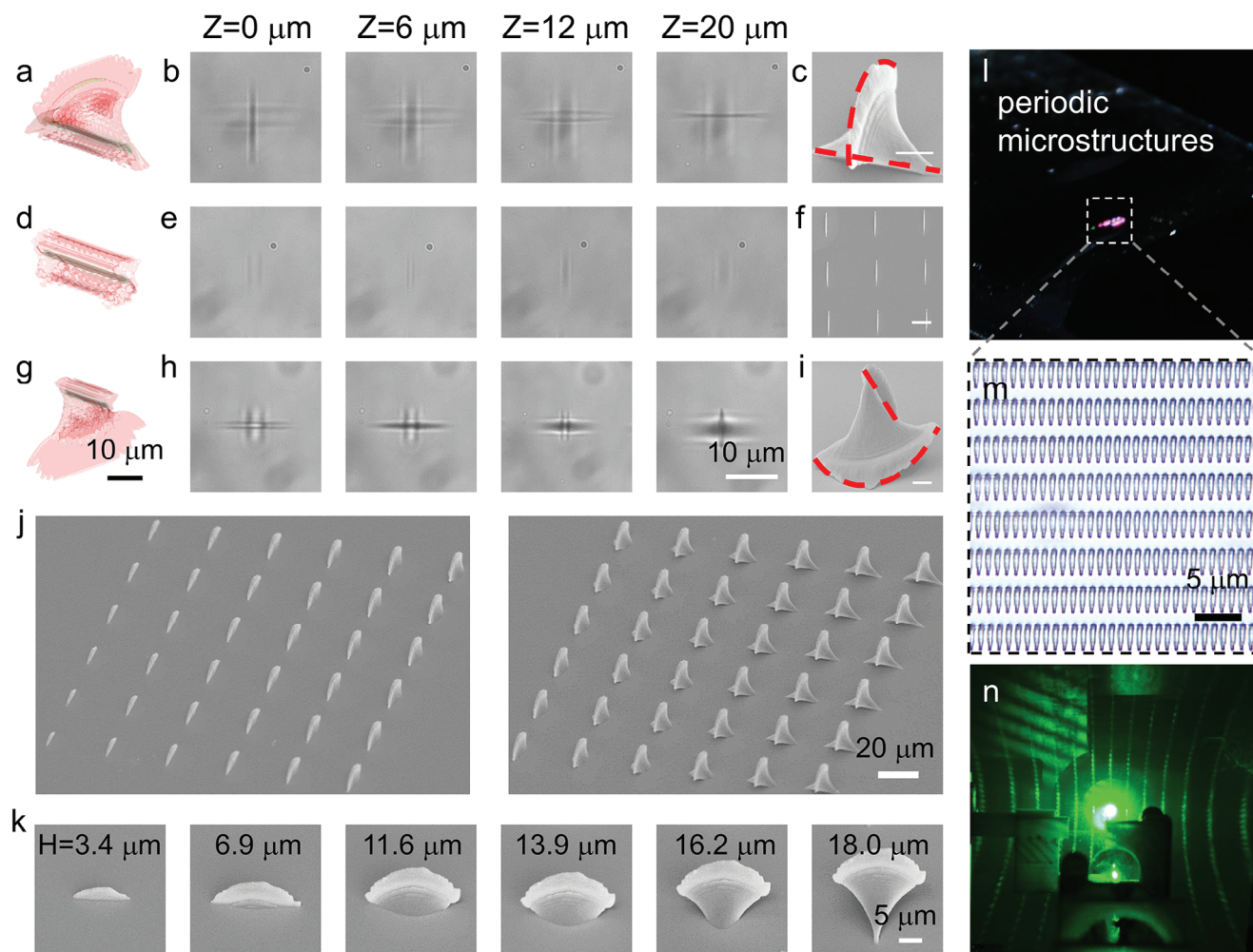
**ADVANCED
SCIENCE NEWS**

www.advancedsciencenews.com

**ADVANCED
FUNCTIONAL
MATERIALS**

www.afm-journal.de

Figure 4. The 3D topography of the DLSF by femtosecond laser two-photon polymerization. a) The simulated 3D shape of DLSF (f = 1000 mm, NA = 1.35). b) The optical images of the microstructure exposed using DLSF (f = 1000 mm) at different z position. c) The SEM images of the dumpling-shaped microstructures fabricated by the DLSF (f = 1000 mm) with a single exposure. d) The simulated 3D shape of DLSF (f = 1600, NA = 1.35). e) The optical images of the microstructure exposed using DLSF (f = 1600) at different Z position. f) The SEM images of the micro dumplings fabricated by the DLSF (f = 1600) single exposure. g) The simulated 3D shape of DLSF (f = 2200 mm, NA = 1.35). h) The optical images of the microstructure exposed using DLSF (f = 2200 mm) at different Z position. i) The SEM images of the micro dumplings fabricated by the DLSF (f = 2200 mm) single exposure. j) The micro dumplings array fabricated by the single exposure of DLSF. k) The SEM images of dumpling-shaped microstructure with different heights. l) The optical images of the fabricated periodic structure. m) The optical microscopic images of the fabricated periodic structure. n) Diffraction pattern taken by laser irradiation of the prepared periodic structure. The scale bar is 5 μm in (c,i). The scale bar of (f) is 10 μm.

and vibration monitoring, with the expectation of achieving high-performance position and vibration sensing using this beam.

The test setup, depicted in **Figure** 5a, features a reflective mirror (RM) positioned beneath the OL. During the test experiments, a nanopiezoelectric platform controls the position of the RM. When the spatial position of the RM is changed, the reflected DLSF can be captured by a CCD. By altering the spatial position of the RM, the reflected DSLF can be captured using a CCD. Subsequently, through computer analysis of the captured beam in the horizontal (X) and vertical (Y) directions, the precise spatial position along the Z-axis can be determined.

To facilitate the data analysis, we define the half-height width of the beam in the x direction as Wx, the half-height width of the beam in the y direction as Wy, and the zero position of the z-axis at Wx = Wy. Figure 5b illustrates typical images of the re-

flected DLSF. At Z = 100 nm, a clearly visible horizontal spot with Wx = 1280 nm and Wy = 638 nm can be observed. When the position is changed to Z = 0 nm, the spot has an equal size of 960 nm in both the horizontal and vertical directions. As the z-coordinate becomes −100 nm, the spot size changes to 1128 and 410 nm in the horizontal and vertical directions, respectively. Subsequently, we quantitatively measured the Wx/Wy of DLSF and the results are shown in Figure 5C. It can be seen that the Wy has a fine linearity and can be further fitted by y = a + bx (a = 934.69594 ± 7.16978 nm, b = −2.37062 ± 0.06518, and R-squared = 0.94). In addition, Wx changes most drastically around z = 0, reaching 19.1 nm for every 1 nm change in Z theoretically, which provides the basis for high-precision position sensing. Besides, it is worth noting that the change in the lateral width of DSLF (Wx) with focus position is opposite to the change in the
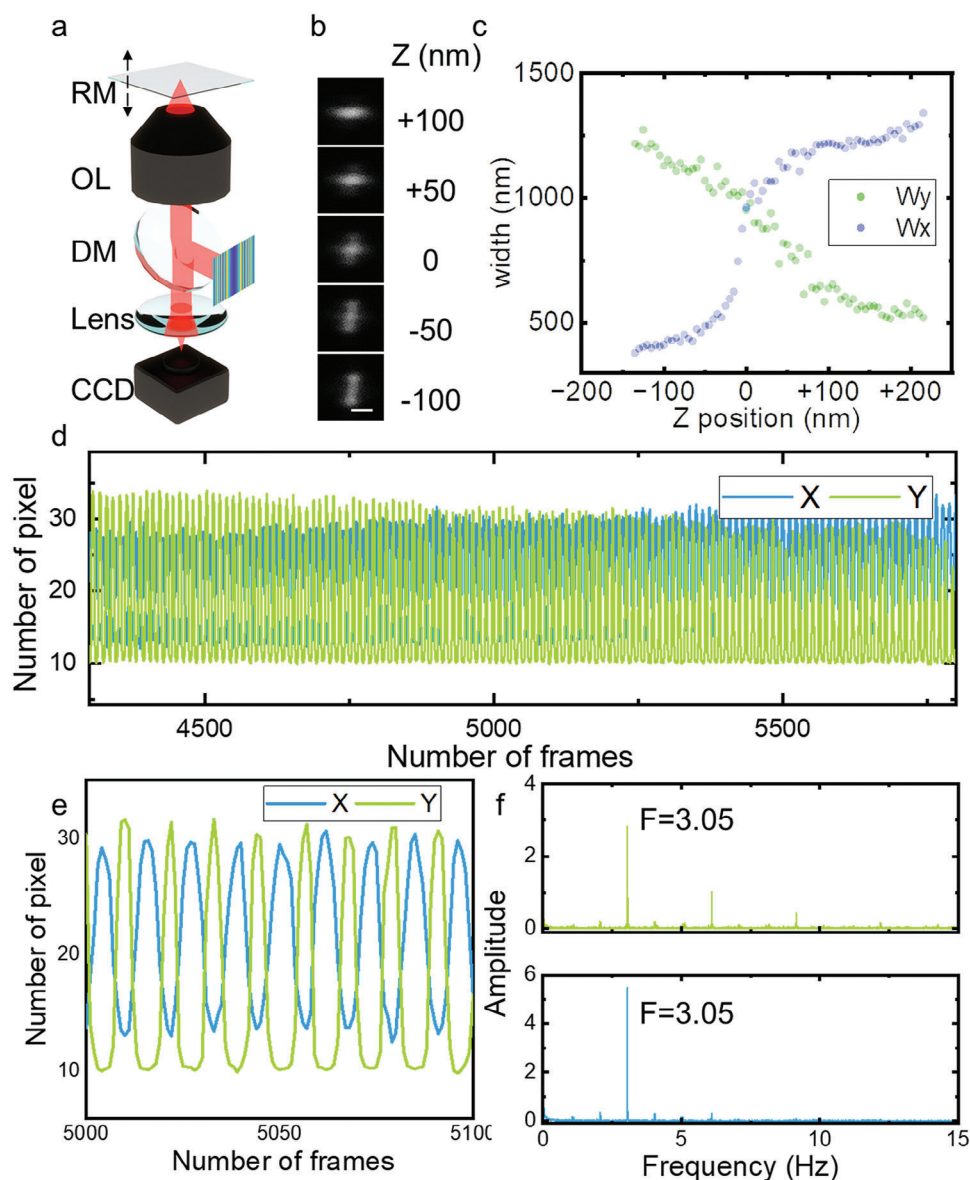
ADVANCED
SCIENCE NEWS

www.advancedsciencenews.com

ADVANCED
FUNCTIONAL
MATERIALS

www.afm-journal.de

Figure 5. The position and vibration test scheme based on DLSF beam. a) The simplified optical diagram for determining the z-coordinate of the measured object by introducing DLSF into the imaging path. b) The DLSF intensity images at different z positions captured by CCD. c) The curve of image reflected spot widths Wx and Wy as a function of z obtained using the incident beam (DLSF, f = 100 mm). d) Vibration test results under excitation amplitude of 500 nm and frequency of 3.05. e) A zoomed-in image of a vibration test result, which well shows the sinusoidal characteristics of the excitation signal. f) The Fourier transform result of the signal Wx and Wy in (c). The results show that the vibration frequency of the object to be tested is 3.05, which is consistent with the frequency of the excitation signal.

longitudinal width of DSLF (Wy) with focus position. This means that when we take Wx = Wy as Z = 0, we can distinguish the positive and negative z position through the state of DSLF. This ability, utilizing the unique 3D light field distribution of 3D DSLF to distinguish positive and negative Z-direction positions, surpasses the capabilities of conventional 2D focusing spots such as Gaussian focus and linear focus.

The measurement accuracy of this method is determined by a variety of environmental factors, the most important of which are two parameters, the vibration of the environment itself and the resolving ability of the optical system. On the one hand, the

position of the RM is controlled by a nanopiezoelectric platform. Despite our best efforts, environmental vibrations (e.g., lasers water cooling, vibrations generated by drive cooling fans) are still inevitable. These factors contribute to minor vibrations at the experimental station. We used the acquisition card to record the absolute spatial position of the platform/RM, and the results showed that the spatial vibration was ≈6–8 nm (Figure S5, Supporting Information), implying that we could not detect position or vibration signals below this threshold. On the other hand, the optical system utilized in this system can resolve changes in the intensity profile full width at half maximum (FWHM) of the spot up
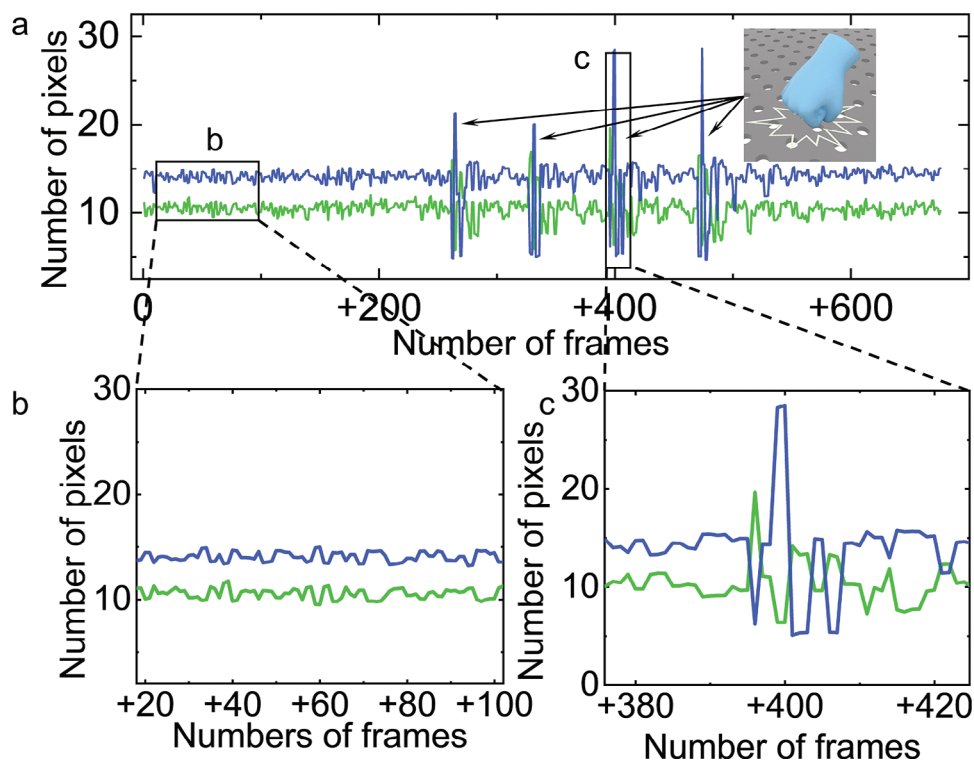
**ADVANCED
SCIENCE NEWS**

www.advancedsciencenews.com

**ADVANCED
FUNCTIONAL
MATERIALS**

www.afm-journal.de

Figure 6. The concept demonstration of micro vibration testing. a) The test results of the vibration of the platform, the inset shows that the tester taps the platform to be tested lightly with hand during the test. b) The system detects a noise level ≈10 nm when no knocking occurs. c) When the hand hits the platform, the test system can sensitively detect the vibration of the platform.

to 200 nm. If we use the half-height width of the spot in the x-direction for position sensing, the theoretical limit of resolution for position sensing would be 10 nm. Therefore, under the existing experimental conditions, the theoretical testing accuracy of this protocol is ≈10 nm, equivalent to 1/80 λ.

This study presents the successful realization of position sensing via the capture and analysis of images generated by the DSLF. Furthermore, it demonstrates the capability of detecting vibrations through continuous image processing. In this context, we showcase the vibration detection potential by applying a periodic sinusoidal voltage signal to the piezoelectric platform and subsequently detecting and analyzing the changes in the actual spots.

The platform's vibration during a single period (amplitude 500 nm, period 0.32764 s, frequency 3.05) is depicted in Figure S6 (Supporting Information). During the test process, one CCD is utilized to capture the images. The captured frames are analyzed in real time by a computer to obtain the value of the FWHW in both the X and Y directions, and the experimental result is shown in Figure 5d. The collected vibration signal exhibits remarkable stability and effectively reflects the sinusoidal vibration pattern of the platform. A closer examination of Figure 5e, focusing on frames 5000–5100, highlights the sinusoidal variation in the measured signal (x/y) over time. Through Fourier analysis of the acquired signal, it can be obtained that the frequency of the measured platform vibration signal is 3.05, which is exactly the same as the given value (Figure 5f), demonstrating the efficacy of the vibration detection method. Besides, we performed a vibration test with preset amplitude of 100 and 10 nm

as shown in Figures S5 and S6 (Supporting Information). When the amplitude is 100 nm, the signal still illustrates the state of the sinusoidal vibration of the platform, and the Fourier analysis shows that the frequency is 3.05 (Figure S7, Supporting Information). However, with 10 nm amplitude, the measured signal exhibits increased noise, and the time-domain results primarily reflect the platform's vibration but not its sinusoidal vibration pattern (Figure S6, Supporting Information). Nevertheless, the frequency domain analysis is still effective in extracting the vibration information of the platform.

The method presented in this paper demonstrates the ability to resolve the 10 nm position and vibration. Compared to the laser Doppler vibrometer method,[34] this method does not require the construction of a complex interference system, offering advantages in terms of stability and cost. Additionally, compared to the laser triangulation method,[35] this proposed approach only requires a single probe (objective lens) to achieve high-precision position measurement. Considering that the test resolution has far exceeded the diffraction limit of optics, and this experiment only needs one CCD to complete the signal processing, we believe that the method proposed in this paper has advantages in terms of comprehensive performance and is advantageous in fields such as vibration sensing and position measurement.

Finally, as a concept demonstration, we use this method to detect the microvibrations caused by hand tapping the optical platform. As showcased in **Figure 6**, when the experimenter gently taps the optical stage, the value of the X and Y direction signals caused by the spot change changes in real time. Figure 6b,c are

typical signal plots where there is no vibration and vibration, respectively, from which it can be seen that the vibration noise of the optical stage is 10 nm, and when struck, the mirror under the objective lens produces a vibration of ≈450 nm, proving that it has potential applications in vibration monitoring and other fields.

3. Conclusion

In this study, we have unveiled a novel optical phenomenon known as the Dumpling-shaped Structured Light Field (DSLF), which is formed when cylindrical lens beams are focused under tight focus conditions. We constructed a spatial light modulator (SLM) assisted optical modulation system for the flexible generation and modulation different typical states of DSLF. Through a comprehensive examination of DSLF, we identified a correlation between the secondary focal point and the phase at the objective lens's entrance pupil, supported by both theoretical analysis and experimental validation, achieving perfect elimination of secondary focus and adjustable 3D DSLF generation. Based on the 3D DSLF modulation technology, we showcased the utility of DSLF in rapid microstructure fabrication via femtosecond laser two-photon polymerization. Besides, benefit from the unique spatial light field distribution of 3D DSLF, we demonstrated the potential of DSLF in nanoscale high-precision optical sensing, with the ability to resolve position changes and vibrations as low as 10 nm, which is difficult to achieve with traditional 2D light fields. This method presents a cost-effective and stable alternative to existing vibration and position sensing techniques. Overall, our research contributes to a deeper understanding of structured light. The DLSF may offer practical applications in various fields, including micro/nano processing, optical imaging, sensing, and beyond.

4. Experimental Section

Femtosecond Laser Two-Photon Polymerization: In this study, a femtosecond laser system consisting of a mode-locked titanium-sapphire oscillator produced by Coherent Inc. was employed. The laser source features an 800 nm center wavelength, a pulse width of 75 femtoseconds, and a repetition rate of 80 MHz. To facilitate this work, a pure phase reflective liquid crystal silicon-based spatial light modulator known (Pluto NIR-2, HOLOEYE) was utilized.

Hologram Generation and Optical Beam Simulations: The spatial light modulator boasts a resolution of 1920×1080 with an 8 µm pixel pitch. During the exposure process, an 8-bit grayscale image with 256 adjustable grayscale levels was employed to modulate the laser wavefront. Holograms, designed as 1080×1080 matrices, were created using the commercial software MATLAB 2018a. The incident beam can be described by the equation $E(x, y) = A(x, y)\exp[i\varphi(x, y)]$, with the phase $\varphi(x, y)$ determined by the cylindrical lens phase $\varphi(x, y) = \frac{2\pi}{\lambda}\frac{x^2}{2f}$. The focused light field simulation was carried out using the mathematical software MATLAB (2018a).

Sample Preparation: A 15 µL hybrid organic–inorganic material photoresist (SZ2080) acquired from IESL-FORTH was utilized. Prior to fabrication, the photoresist was deposited onto a cleaned 20 mm × 20 mm glass slide and heated at 100 °C for 60 min. After fabrication, the entire sample was immersed in propanol acetone for 30 min to remove unprocessed areas. Subsequently, the sample was air-dried to prepare it for the assembly of 3D chiral microstructures.

Characterization: Scanning electron microscope (SEM) images were captured using a Zeiss EVO18, while optical images were obtained using

a Leica DMI3000B optical microscope. Precise control over the movement was achieved using a nano-positioning stage (Physik Instrumente E545) with nanometer resolution and a 200 µm movement range.

Supporting Information

Supporting Information is available from the Wiley Online Library or from the author.

Conflict of Interest

The authors declare no conflict of interest.

Author Contributions

D.P., J.Z., Z.W., S.Z., B.Y., and D.W. designed the experiments. D.P., Z.F., H.W., C.Z., Z.L., J.N., Y.K., B.X. performed the experiments. J.Z. and DP. did the light field calculation work. D.P. and Z.W. wrote the manuscript.

Data Availability Statement

The data that support the findings of this study are available from the corresponding author upon reasonable request.

[1] N. G. Orji, M. Badaroglu, B. M. Barnes, C. Beitia, B. D. Bunday, U. Celano, R. J. Kline, M. Neisser, Y. Obeng, A. E. Vladar, *Nat. Electron.* **2018**, *1*, 532.

[2] M. Krieg, G. Fläschner, D. Alsteens, B. M. Gaub, W. H. Roos, G. J. L. Wuite, H. E. Gaub, C. Gerber, Y. F. Dufrêne, D. J. Müller, *Nat Rev Phys* **2019**, *1*, 41.

[3] B. P. Abbott, R. Abbott, T. D. Abbott, M. R. Abernathy, F. Acernese, K. Ackley, C. Adams, T. Adams, P. Addesso, R. X. Adhikari, V. B. Adya, C. Affeldt, M. Agathos, K. Agatsuma, N. Aggarwal, O. D. Aguiar, L. Aiello, A. Ain, P. Ajith, B. Allen, A. Allocca, P. A. Altin, S. B. Anderson, W. G. Anderson, K. Arai, M. A. Arain, M. C. Araya, C. C. Arceneaux, J. S. Areeda, N. Arnaud, et al., *Phys. Rev. Lett.* **2016**, *116*, 061102.

[4] M. J. Biercuk, H. Uys, J. W. Britton, A. P. VanDevender, J. J. Bollinger, *Nat. Nanotechnol.* **2010**, *5*, 646.

[5] S. M. Yang, G. F. Zhang, *Meas. Sci. Technol.* **2018**, *29*, 102001.

[6] M. Neugebauer, P. Wozniak, A. Bag, G. Leuchs, P. Banzer, *Nat. Commun.* **2016**, *7*, 11286.

[7] Z. Xi, H. P. Urbach, *Phys. Rev. Lett.* **2017**, *119*, 053902.

[8] B. Reynier, E. Charron, O. Markovic, X. Yang, B. Gallas, A. Ferrier, S. Bidault, M. Mivelle, *Optica* **2023**, *10*, 841.

[9] G. H. Yuan, N. I. Zheludev, *Science* **2019**, *364*, 771.

[10] T. Zang, H. Zang, Z. Xi, J. Du, H. Wang, Y. Lu, P. Wang, *Phys. Rev. Lett.* **2020**, *124*, 243901.

[11] a) H. F. Zang, Z. Xi, Z. Y. Zhang, Y. H. Lu, P. Wang, *Sci. Adv.* **2022**, *8*, eadd1973; b) H. Zang, Z. Zhang, Z. Huang, Y. Lu, P. Wang, *Sci. Adv.* **2024**, *10*, eadk2265.

[12] C. He, Y. Shen, A. Forbes, *Light Sci Appl* **2022**, *11*, 205.

[13] A. Forbes, M. de Oliveira, M. R. Dennis, *Nat. Photonics* **2021**, *15*, 253.

[14] H. Rubinsztein-Dunlop, A. Forbes, M. V. Berry, M. R. Dennis, D. L. Andrews, M. Mansuripur, C. Denz, C. Alpmann, P. Banzer, T. Bauer, E. Karimi, L. Marrucci, M. Padgett, M. Ritsch-Marte, N. M. Litchinitser, N. P. Bigelow, C. Rosales-Guzmán, A. Belmonte, J. P. Torres, T. W. Neely, M. Baker, R. Gordon, A. B. Stilgoe, J. Romero, A. G. White, R. Fickler, A. E. Willner, G. Xie, B. McMorran, A. M. Weiner, *J Opt* **2017**, *19*, 013001.

[15] Y. Shen, X. Wang, Z. Xie, C. Min, X. Fu, Q. Liu, M. Gong, X. J. L. S. Yuan, *Applications* **2019**, *8*, 90.

[16] P. Vaity, L. Rusch, *Opt. Lett.* **2015**, *40*, 597.

[17] G. A. Siviloglou, J. Broky, A. Dogariu, D. N. Christodoulides, *Phys. Rev. Lett.* **2007**, *99*, 213901.

[18] A. Vella, S. T. Head, T. G. Brown, M. A. Alonso, *Phys. Rev. Lett.* **2019**, *122*, 123603.

[19] a) A. H. Dorrah, P. Bordoloi, V. S. de Angelis, J. O. de Sarro, L. A. Ambrosio, M. Zamboni-Rached, F. Capasso, *Nat. Photonics* **2023**, *17*, 427; b) L. Chen, J. Lei, J. Romero, *Light: Sci. Appl.* **2014**, *3*, e153; c) P. F. Liu, T. Z. Shi, H. W. Li, H. Y. Chen, Y. Huang, H. Z. Ma, T. Y. Zhu, R. Zhao, Y. Li, Q. Xin, L. Liu, S. Sun, H. M. Nie, W. Long, H. Wang, J. W. Wang, X. D. Zhang, D. Ming, *Nano Today* **2022**, *47*, 101628.

[20] S. K. Noor, M. N. M. Yasin, A. M. Ismail, M. N. Osman, P. J. Soh, N. Ramli, A. H. Rambe, *Ieee Access* **2022**, *10*, 89465.

[21] Q. Q. Zhang, C. K. Pang, L. Yang, Z. H. Li, H. Y. Huang, G. Wu, *IEEE Photonics J* **2022**, *14*, 1.

[22] H. Guo, J. F. Yan, L. Jiang, S. F. Deng, X. Z. Lin, L. T. Qu, *ACS Appl. Mater. Interfaces* **2022**, *14*, 39220.

[23] Z. Wang, L. Miccio, S. Coppola, V. Bianco, P. Memmolo, V. Tkachenko, V. Ferraro, E. Di Maio, P. L. Maffettone, P. Ferraro, *Light: Advanced Manufacturing* **2022**, *3*, 151.

[24] R. Barboza, A. Babazadeh, L. Marrucci, F. Cardano, C. de Lisio, V. D'Ambrosio, *Nat. commun.* **2022**, *13*, 1080.

[25] C. Zuo, J. Qian, S. Feng, W. Yin, Y. Li, P. Fan, J. Han, K. Qian, Q. Chen, *Light Sci Appl* **2022**, *11*, 39.

[26] C. J. R. Sheppard, *Appl. Opt.* **2013**, *52*, 538.

[27] S. Huang, P. Wang, X. Shen, J. Liu, R. Li, *Optica* **2022**, *9*, 469.

[28] K. M. Dean, T. Chakraborty, S. Daetwyler, J. L. Lin, G. Garrelts, O. M'Saad, H. T. Mekbib, F. F. Voigt, M. Schaettin, E. T. Stoeckli, F. Helmchen, J. Bewersdorf, R. Fiolka, *Nat. Protoc.* **2022**, *17*, 2025.

[29] L. Chen, K. Q. Cao, Y. L. Li, J. K. Liu, S. Zhang, D. H. Feng, Z. R. Sun, T. Q. Jia, *Opto-Electron. Adv.* **2021**, *4*, 230013.

[30] L. Wang, Q. D. Chen, X. W. Cao, R. Buividas, X. W. Wang, S. Juodkazis, H. B. Sun, *Light Sci Appl* **2017**, *6*, e17112.

[31] a) Y. Yang, A. Forbes, L. Cao, *Opto-Electron. Sci.* **2023**, *2*, 230026; b) X. Zang, Z. Liu, Y. Xu, Y. Wang, Q. Wang, Z. Li, L. Wang, *Science China Technological Sciences* **2023**, *67*, 60; c) H. Wang, W. Zhang, D. Ladika, H. Yu, D. Gailevičius, H. Wang, C. F. Pan, P. N. S. Nair, Y. Ke, T. Mori, J. Y. E. Chan, Q. Ruan, M. Farsari, M. Malinauskas, S. Juodkazis, M. Gu, J. K. W. Yang, *Adv. Funct. Mater.* **2023**, *33*, 2214211; d) A. Balena, M. Bianco, F. Pisanello, M. De Vittorio, *Adv. Funct. Mater.* **2023**, *33*, 2211773; e) W. Ouyang, X. Xu, W. Lu, N. Zhao, F. Han, S. C. Chen, *Nat. Commun.* **2023**, *14*, 1716; f) G. Liu, B. Chen, Z. Tian, Q. Zhong, S.-C. Chen, *Opt. Express* **2024**, *32*, 17143.

[32] a) L. Wang, Q. D. Chen, X. W. Cao, R. Buividas, X. Wang, S. Juodkazis, H. B. Sun, *Light Sci Appl* **2017**, *6*, e17112; b) T. Zou, B. Zhao, W. Xin, Y. Wang, B. Wang, X. Zheng, H. Xie, Z. Zhang, J. Yang, C. L. Guo, *Light Sci Appl* **2020**, *9*, 69; c) K. Xu, L. Huang, S. Xu, *Optica* **2023**, *10*, 97; d) J. Huang, L. Jiang, X. Li, Q. Wei, Z. Wang, B. Li, L. Huang, A. Wang, Z. Wang, M. Li, L. Qu, Y. Lu, *Adv. Opt. Mater.* **2019**, *7*, 1900706; e) H. Li, B. Yang, M. Wang, C. Gao, B. Wu, L. Zeng, X. Xi, Z. Chen, X. Wang, Z. Wang, J. Chen, *APL Photonics* **2023**, *8*, 046101; f) K. Xu, L. Huang, X. Zhou, M. Zheng, M. Wang, S. Xu, *Opt. Lett.* **2024**, *49*, 1778; g) J. Qiao, J. Huang, L. Zhao, D. Yuan, P. Wang, S. Xu, *Adv. Mater. Technol.* **2022**, *8*, 2201209; h) H. Li, G. Liu, Q. Zhong, S. C. Chen, *Opt. Express* **2024**, *32*, 2347.

[33] a) D. Pan, S. L. Liu, J. W. Li, J. C. Ni, C. Xin, S. Y. Ji, Z. X. Lao, C. C. Zhang, B. Xu, R. Li, S. Y. Fan, P. J. Li, Y. L. Hu, D. Wu, J. R. Chu, *Adv. Funct. Mater.* **2022**, *32*, 2106917; b) D. Pan, B. Xu, S. Liu, J. Li, Y. Hu, D. Wu, J. Chu, *Opt. Lett.* **2020**, *45*, 2584.

[34] S. J. Rothberg, M. S. Allen, P. Castellini, D. Di Maio, J. J. J. Dirckx, D. J. Ewins, B. J. Halkon, P. Muyshondt, N. Paone, T. Ryan, H. Steger, E. P. Tomasini, S. Vanlanduit, J. F. Vignola, *Optics and Lasers in Engineering* **2017**, *99*, 11.

[35] a) D. W. Ding, W. F. Ding, R. Huang, Y. C. Fu, F. Y. Xu, *Measurement* **2023**, *216*, 113001; b) M. F. M. Costa, *Opt. Eng.* **1996**, *35*, 2743.